Proceedings of the 11th Australasian Heat and Mass Transfer Conference, AHMTC11
9-10th July 2018, RMIT University, Melbourne, Australia

11AHMTC18-30

THE EFFECT OF CENTRIFUGAL BUOYANCY ON ROTATING HORIZONTAL CONVECTION

Tony Vo and Gregory J. Sheard
The Sheard Lab, Department of Mechanical and Aerospace Engineering, Monash University, Melbourne, Australia

ABSTRACT

The Boussinesq approximation considers density variations due to the gravitational buoyancy, and is commonly used to model natural convection. However, this approximation neglects centrifugal buoyancy effects which have been shown to play a significant role in the flow development and stability of rapidly-rotating flows, such as those present in astrophysical and geophysical systems. Thus, this paper investigates the centrifugal buoyancy effects in rotating horizontal convection.

This numerical study considers a rotating cylindrical tank subjected to a linear temperature gradient extending radially over the base. The flow is governed by the time-dependent Navier–Stokes equations coupled with a thermal-transport equation, incorporating centrifugal buoyancy terms. A high-order spectral-element solver is used to compute the axisymmetric base-flow solutions for a range of governing parameters including the Rayleigh number Ra, rotational parameter Q, and Froude number Fr. Suppression of convection is observed with increasing Q as expected. In contrast, variations in Fr demonstrate enhanced heat transfer due to centrifugal buoyancy effects under appropriate flow conditions.

1 INTRODUCTION

Horizontal convection (HC) is a class of flow induced by a variation of temperature imposed along a horizontal boundary in a fluid-filled enclosure. The key resulting feature from this forcing is a large-scale overturning circulation which is particularly relevant to geophysical, industrial and astrophysical systems [1]. An example is the differential heating along the ocean's surface (from equator to pole). Thus, HC is typically used as a simple model to study the dynamics, heat transport, and dissipation properties of buoyancy driven flows.

The study of HC primarily comprises of two branches: planar and rotating. Extensive literature concerning the effect of thermal forcing, aspect ratio and fluid properties on planar HC in rectangular enclosures exists [2,3], including the stability properties of the flow [4]. HC transitions through several regimes as the Rayleigh number is increased. The Rayleigh number, Ra, describes the ratio between buoyancy and viscous forces. At low Rayleigh numbers, the flow is diffusion dominated and described by a near-symmetrical overturning circulation created by cooler flow travelling along the base towards the hotter boundary. Buoyant destabilisation drives the fluid above the hotter boundary upwards along the sidewall and completes the circulation once it sinks due to the cooler forcing. Convection begins to set in above a critical Rayleigh number where plumes develop over the hotter region of the boundary. The pioneering work by [5] determined a Nusselt number scaling of $Nu \propto Ra^{1/5}$ in this convective regime which has been supported in subsequent HC studies [2,3,6]. The flow begins to become unsteady as the Rayleigh number continues to increase.

Similar aspects of planar HC have been studied for rotating HC, although to a lesser extent [7–10]. The addition of rotation to the HC system introduces an Ekman layer which forms over the base. The square of the ratio of the thermal and Ekman layer thicknesses, denoted as the rotation parameter Q, is useful in characterising the flow. Reference [9] categorises the flow into three regimes as follows: weak rotation (regime III, $0 < Q < 1$), strong rotation (regime II, $1 \ll Q \ll Ra^{4/15}$) and very strong rotation (regime I, $Q \gg Ra^{4/15}$). These categories are coincident with the six regimes proposed by [7]. Reference [9] showed that for weak rotation ($Q < 1$) the flow exhibits the same scaling as the non-rotating case such that $Nu \propto Ra^{1/5}$. However, increasing the rotation to moderate values ($Q > 1$) suppresses the onset of convection and causes the scaling to deviate from the 1/5 exponent.

Numerical simulations of HC to date typically adopt the Boussinesq approximation to model density variations only in terms in the governing equation which involve accelerations due to gravity. This traditional approach of the approximation is widely used to model thermal convection in both non-rotating and rotating flows. However, centrifugal buoyancy may have significant effects in rapidly rotating flows with differential rotation or strong eddies as it directly affects the upwards advection of the basic-state vertical shear by the perturbation rolls and modifies the mean thermal stratification [11]. Reference [12] proposes a new Boussinesq-type approximation that incorporates centrifugal buoyancy by retaining density variations in the advection term of the Navier–Stokes equations. The study demonstrates discrepancies in critical values between the traditional and new approximations for Taylor–Couette flow, as well as illustrating traditional effects to be qualitatively incorrect under certain conditions.

The effect of centrifugal buoyancy in rotating Rayleigh–Bénard convection and Taylor–Couette configurations have been studied previously, but not in rotating horizontal convection. Hence, this paper addresses the effect of centrifugal buoyancy in rotating HC by characterising the axisymmetric base flows for a wide range of governing parameters.

2 METHODOLOGY

2.1 PROBLEM DESCRIPTION

This paper investigates flow in a cylindrical enclosure with a radius R and height H rotating at angular velocity Ω. The aspect ratio is fixed at $A = H/L = 0.4$ in this study, following [9] and [10]. A schematic of the system is shown in Figure 1.

The enclosure is filled with a fluid of kinematic viscosity ν, thermal diffusivity κ, volumetric expansion coefficient α, and density ρ. The base ($z = 0$) and sidewalls ($z = R$) rotate at an angular velocity while the top boundary ($z = H$) is treated as a stress-free surface. A linearly increasing temperature profile is imposed on the base while all other boundaries are thermally insulated.

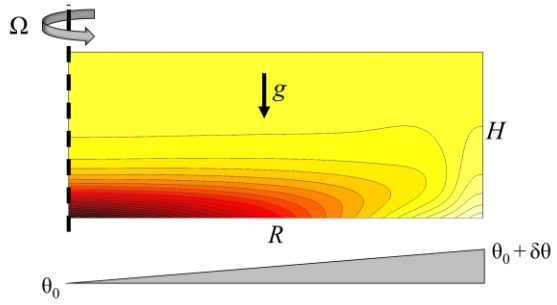

Figure 1: A schematic diagram illustrating the following key parameters in the semi-meridional domain: tank radius R, tank height H, gravity vector $\mathbf{g}$, rotation rate Ω, and the linear temperature profile imposed along the base of the tank which varies from a reference temperature θ_0 to $\theta_0 + \delta\theta$. The cylindrical coordinate system is adopted where (r, φ, z) denotes the radial, azimuthal and upward directions, respectively. The origin is located at the point where the axis of rotation and base coincide. The contours represent temperature with dark and light contours representing low and high values, respectively.

2.2 GOVERNING EQUATIONS AND PARAMETERS

The time-dependent Navier–Stokes equations coupled with a thermal transport equation through a Boussinesq approximation, including centrifugal buoyancy effects, are used to describe the rotating HC flow. By normalising lengths by R, velocity by ΩR, time by $1/\Omega$, pressure by $\rho R^2\Omega^2$ and temperature by $\delta\Omega$, the governing equations in non-dimensional form are written as

$$\frac{\partial \mathbf{u}}{\partial t} = -(\mathbf{u}\cdot\nabla)\mathbf{u} - \nabla p + \frac{2}{QRa^{2/5}}\nabla^2\mathbf{u} - \frac{4Ra^{1/5}}{PrQ^2}\theta[\hat{\mathbf{g}} - Fr(\mathbf{u}\cdot\nabla)\mathbf{u}], \tag{1a}$$

$$\frac{\partial \theta}{\partial t} = -(\mathbf{u}\cdot\nabla)\theta + \frac{2}{PrQRa^{2/5}}\nabla^2\theta, \tag{1b}$$

$$\nabla\cdot\mathbf{u} = 0, \tag{1c}$$

where $\mathbf{u}$ is the velocity vector, t is time, p is pressure, and $\hat{\boldsymbol{g}}$ is a unit vector in the direction of gravity (negative y direction). The non-dimensional parameters Q (rotational parameter), Ra (horizontal Rayleigh number), Pr (Prandtl number), and Fr (Froude number) are respectively defined as

$$Q = \frac{1}{ERa^{2/5}A^2}, \tag{2a}$$

$$Ra = \frac{g\alpha\delta\theta R^3}{\nu\kappa}, \tag{2b}$$

$$Pr = \frac{\nu}{\kappa}, \tag{2c}$$

$$Fr = \frac{R\Omega^2}{g}, \tag{2d}$$

where E is the Ekman number representing the balance between viscous and Coriolis effects [7]. The Ekman number is defined as

$$E = \frac{\nu}{2\Omega H^2}. \tag{3}$$

The rotational parameter Q characterises the importance of rotation in the system through the square of the ratio of boundary layer thicknesses (thermal to Ekman layers). Rotation is considered important when $Q > \mathcal{O}(1)$ and corresponds to the thermal boundary layer being thicker than the Ekman layer. In contrast, viscous dissipation is considered dominant when $Q < \mathcal{O}(1)$ and corresponds to the Ekman layer being thicker than the thermal boundary layer. Reference [7] uses the Q parameter to classify six different regimes, ranging from no rotation ($Q = 0$) to very strong rotation ($Q \gg Ra^{4/5}$). This study focuses on $Q = 1$.

The convective heat transfer through the base can be characterised by the Nusselt number Nu, which is defined as

$$Nu = \left|\frac{\overline{\partial\theta}}{\partial z}\right|\frac{R}{\delta\theta}, \tag{4}$$

where $\left|\overline{\partial\theta/\partial z}\right|$ is the integral of the absolute value of temperature flux over the base. It should be noted that (4) does not follow $Nu \to 1$ for diminishing convection as the definition is the relativity of vertical heat flux with horizontal conduction.

Rayleigh numbers ranging $10^1 \le Ra \le 10^9$ are explored to capture diffusion and convective-dominant regimes. The Prandtl number is fixed at $Pr = 6.14$ to represent water at laboratory conditions. The Froude number is varied through $0 \le Fr \le 10$ to observe the effect of centrifugal buoyancy in the system.

2.3 NUMERICAL TREATMENT

A nodal spectral-element method is used to spatially discretise the non-dimensional governing equations (1). High-order Gauss–Lobatto–Legendre polynomials are used as interpolants within each macro element, which can be varied to control the spatial resolution. A third-order accurate operator splitting scheme based on backwards differentiation is performed to integrate the governing equations through time. These techniques have been described in detail by [13] and [14]. The present code has been successfully implemented on buoyancy-driven flows in both cylindrical [9,10] and Cartesian formulations [4,15].

2.4 GRID INDEPENDENCE

To ensure grid independence, the convergence of several parameters with increasing element polynomial order N_p, has been computed for several flow conditions. Three parameters for convergence are adopted: measure of L_2 norm of velocity, integral of the temperature within the domain, and Nu. The first two parameters represent global measures while the third represents errors localised at the forcing boundaries, and therefore are considered the most significant.

Typical results are shown in Figure 2 for $Ra = 10^8$, $Q = 1$ and $Fr = 0.1$. The results demonstrate a decreasing error with increasing N_p. A threshold criterion of $\mathcal{O}(10^{-2})$ is sought to ensure that solution error due to finite spatial resolution is much smaller than likely laboratory sources of error. This criterion is satisfied for all measures with $N_p \geq 6$. Hence, this study adopts a minimum of $N_p = 6$.

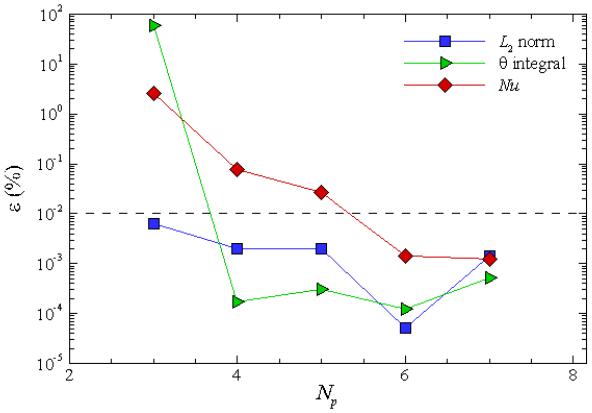

Figure 2: The relative percentage error ε (relative to $N_p = 8$) in the measure of L_2 norm (square), integral of the temperature within the domain (triangle), and Nu (diamond), for $Ra = 10^8$, $Q = 1$ and $Fr = 0.1$.

3 RESULTS AND DISCUSSION

3.1 FLOW FEATURES AND *NU* MEASUREMENTS

Axisymmetric solutions have been obtained primarily for the parameter space $10 \leq Ra \leq 10^9$, and $0 \leq Fr \leq 10$, with $Q = 1$. Time-evolved solutions are considered to be steady when velocity and temperature variations between successive time steps are each smaller than 10^{-10} and 10^{-9}, respectively.

Contours of relative azimuthal velocity $u_{\varphi,\mathrm{rel}}$ (relative to the tank rotation) and temperature are shown in Figure 3, for $Fr = 0$ at various Ra. As expected, at low Ra the θ contours are largely vertical along the base with gradual variations throughout the enclosure due to the flow being diffusion dominated. The corresponding $u_{\varphi,\mathrm{rel}}$ contours show the majority of the flow moving faster than the tank rotation with slower-rotating fluid existing along the base of the enclosure. These characteristics resemble regime-I flows as described by [9] and are typical of what is observed in non-rotating (and weakly rotating) horizontal convection [8,10]. Also, this solution is representative of $Fr \leq 10$ cases as centrifugal buoyancy was found to play a negligible role in diffusion-dominated flows at these Froude numbers. However, there are important differences in $u_{\varphi,\mathrm{rel}}$ that influences Nu, which will be described later for higher Ra where the effect is more apparent.

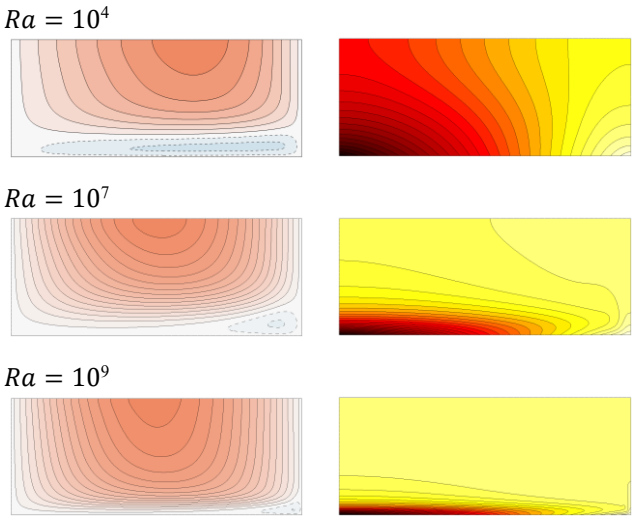

Figure 3: Contours of (left) azimuthal velocity relative to the tank rotation $u_{\varphi,\mathrm{rel}}$, and (right) temperature θ, for $Q = 1$ and $Fr = 0$ at $Ra = 10^4$, 10^7 and 10^9. Contours of temperature with dark and light contours represent low and high values, respectively. Dashed and solid contour lines represent negative and positive contours, respectively.

Increasing Ra causes the isotherms to deviate away from the vertical and incline towards the axis of rotation, while the slower-rotating fluid decreases in volume. At $Ra = 10^9$, a very thin thermal boundary layer has developed with strong stratification in the vertical direction. Features of a high Ra flow resemble those exhibited by regime-III flows, as described by [9].

Figure 4 illustrates the Nusselt number values against Ra for various Fr. At low Rayleigh numbers ($Ra \leq 10^4$), the flow is diffusion dominated and therefore the Nusselt numbers remain

constant at $Nu \approx 2.18$ for all Fr. Nu begins to increase when $Ra > 10^4$ and displays a strong dependence on Fr. The base case of $Fr = 0$ demonstrates a $Nu \propto Ra^{1/5}$ scaling at high Ra, a result which was obtained by [9] through a scaling analysis of the governing equations and via numerical simulations. This is the same scaling observed in planar horizontal convection [5]. Additionally, an equivalent scaling can be derived for $Q = 1$ using the thermal boundary layer thickness relationships presented by [16] and [17]. That is, $Nu \propto Q^{-3/4}Ra^{1/5}$ and $Nu \propto Q^{-1/3}Ra^{1/5}$, respectively. The former scaling has been found to be more appropriate over $1 \lesssim Q \lesssim 10$ by [10]. However, this scaling is lost as Fr begins to increase and no clear power law is identified over this parameter range.

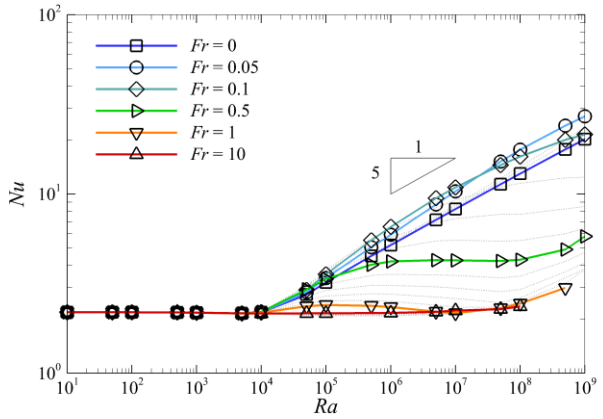

Figure 4: *Nu*-*Ra* curves for various *Fr* values with $Q = 1$. Solid curves denote highlighted *Fr* cases as shown in the legend, while dotted curves illustrate trends of intermediate *Fr* values.

With increasing Fr at a fixed Ra, the flow exhibits Nu increasing to a maximum, then rapidly decreasing to a minimum before remaining relatively constant. This is illustrated in Figure 5. It is found that the maximum Nu points for $Ra \geq 10^4$ demonstrates a relationship of $Nu_{max} = Fr^{-1}$ for $Q = 1$, as represented by the by the dashed-dot-dot line. Additionally, the maximum Nu data exhibits the relationship $Nu_{max} \propto Ra^{0.2265}$. Hence, a larger Ra flow will achieve its maximum Nu at smaller Fr. The solutions corresponding to maximum Nu are all steady state and it is unclear whether these relationships hold for unsteady flows found at higher Ra. Indeed, unsteady axisymmetric solutions have been obtained, albeit not at conditions achieving maximum Nu. The minimum Nu points appear to occur at $Fr \approx 1$ for all Ra, a condition signifying the centrifugal force being stronger than or comparable to the gravitational force.

The Fr corresponding to the minimum and maximum Nu, denoted as $Fr_{Nu,min}$ and $Fr_{Nu,max}$, respectively. These conditions exhibit key features in the flow. The contours for various Fr at $Ra = 10^8$ are shown in Figure 6, noting that $Fr_{Nu,max} \approx 0.05$ and $Fr_{Nu,min} \approx 1$. For $Fr < Fr_{Nu,max}$, fluid in the vicinity of the base travels toward the heated-end of the enclosure as expected, while the interior is dominated is dominated by azimuthal velocities that are stronger than the tank rotation. Also, a thermal boundary layer develops with a strong stratification in the vertical direction which quickly plateaus in the interior.

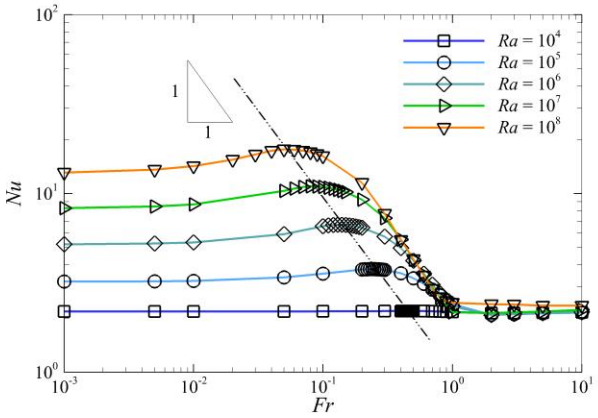

Figure 5: *Nu*-*Fr* curves for various *Ra* values with $Q = 1$.

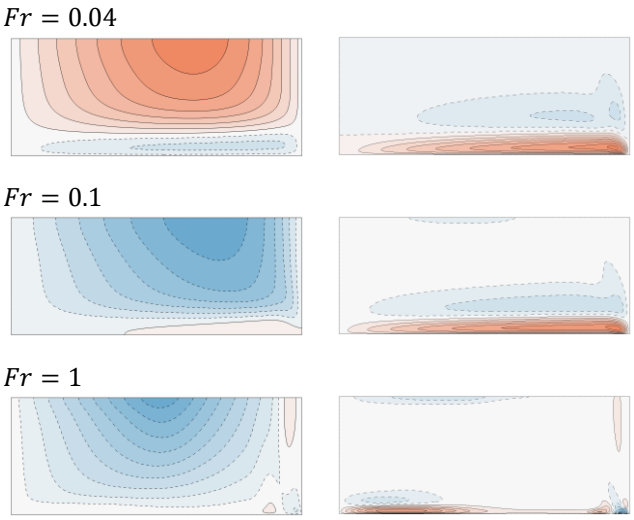

Figure 6: Contours of (left) azimuthal velocity relative to the tank rotation and (right) radial velocity for $Fr = 0.04$, 0.1 and 1 are shown for $Ra = 10^8$ and $Q = 1$. Dashed and solid contour lines represent negative and positive contours, respectively.

The flow maintains positive radial velocities along the entire base as $Fr \rightarrow Fr_{Nu,max}$ and causes a thicker region of flow to exhibit negative $u_{\varphi,rel}$ to develop. Most importantly, the stronger effect of centrifugal buoyancy causes the flow to reach a state of solid-body rotation as $Fr \rightarrow Fr_{Nu,max}$. Consequently, the heat transfer through the base is maximised as there is no minimal azimuthal motion disrupting the flow development in the meridional plane. The flow reintroduces non-zero $u_{\varphi,rel}$ with increasing Fr whereby the boundary layer and interior fluid rotates faster and slower than the tank, respectively.

Correspondingly, the *Nu* is observed to decrease for $Fr_{Nu,\max} < Fr < Fr_{Nu,\min}$.

Significant changes in the flow are observed for $Fr \geq Fr_{Nu,\min}$, where *Nu* remains relatively constant. Firstly, an additional region of faster-rotating fluid near the sidewall begins to develop and eventually extends the entire depth of the tank (see Figure 6, $Fr = 1$). The fluid in these regions are most susceptible to baroclinic instability, seeking different equilibrium positions due to the uneven heating along the base. These characteristics are typical of what is observed in rotation-dominated flows [8,10]. Lastly, the velocity boundary-layer thickness has decreased, and negative radial velocities have emerged along the base near the sidewall.

3.1 Thermal and velocity boundary layer thicknesses

It is also found that the maximum *Nu* is achieved when the velocity-boundary layer thickness δ_u, is at its thickest while the thermal boundary-layer thickness δ_θ, is at its thinnest. The velocity boundary-layer thickness is measured from the bottom wall to the height that corresponds to the nearest local minimum/maximum in the profile of radial velocity. The thermal boundary-layer thickness is measured from the bottom wall to where the temperature first achieves 95% of the temperature at the surface. The thermal and velocity profiles are extracted at mid-radius ($r = 0.5$) across the entire depth of the tank, following the approaches of [9] and [10]. The velocity and thermal boundary-layer thicknesses are shown in Figure 7.

Increasing $Fr \rightarrow Fr_{Nu,\max}$ for a constant *Ra* causes δ_u to increase as shown in Figure 7 (top). The dash-dot-dot line represents the maximum δ_u and exhibits the relationship $\delta_{u,\max} \propto Fr^1$. Therefore, the heat transfer in the system scales linearly with the reciprocal of the velocity boundary layer thickness in the convective regime (i.e. $Ra \geq 10^5$). Further increasing $Fr > Fr_{Nu,\max}$ causes δ_u to decrease at two distinct stages. The range $Fr_{Nu,\max} < Fr < Fr_{Nu,\min}$ exhibits δ_u varying approximately with $Fr^{-1/3}$ and with $Fr^{-1/2}$ thereafter. No clear changes in flow behaviour is observed despite the change in *Fr* scaling exponent beyond $Fr = 1$.

The thermal boundary-layer thickness demonstrates different behaviour to δ_u as shown in Figure 7 (bottom). There is a decrease in δ_θ as $Fr \rightarrow Fr_{Nu,\max}$ due to the increased effect of rotation, causing strong stratification in the vicinity of the base as illustrated by the concentration of isotherms in (see Figure 3). Increases in δ_θ is observed in the intermediate regime $Fr_{Nu,\max} < Fr < Fr_{Nu,\min}$ where the concentrated isotherms begin to deviate away from the axis of rotation towards the top surface. The thermal boundary-layer thickness does not display a consistent power-law dependence on *Fr* across the Rayleigh numbers studied here. The flow eventually becomes diffusion dominated at very-high *Fr* conditions and therefore does not reveal a clear thermal boundary layer (see Figure 7). This explains, in part, the overlaying of δ_θ values at high *Fr* for various *Ra*.

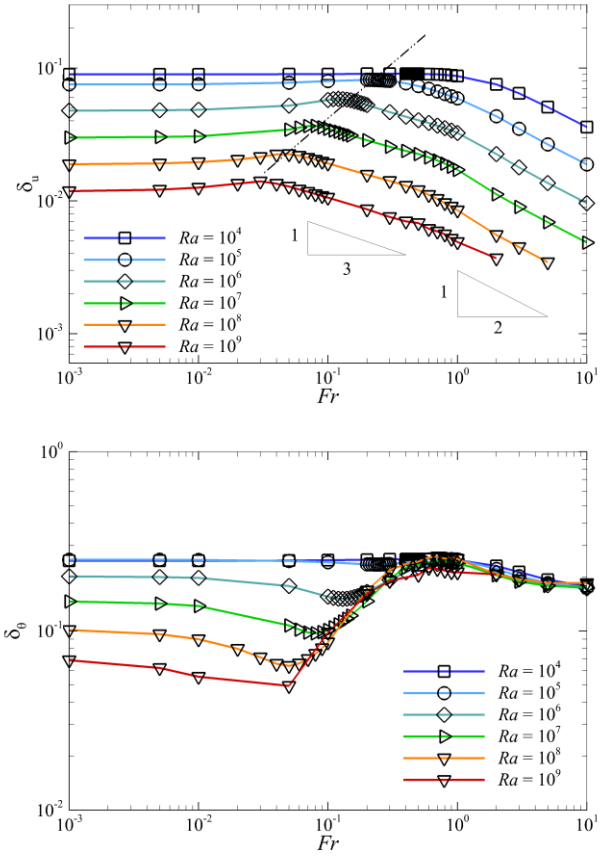

Figure 7: (Top) Velocity and (bottom) thermal boundary-layer thicknesses plotted against *Fr* at $Q = 1$.

4 CONCLUSIONS

This paper investigated the effect of centrifugal buoyancy in rotating horizontal convection. The results show that centrifugal buoyancy effects due to rotation may enhance convective features under the appropriate conditions. Variations in the Froude number demonstrated significant differences in the convective heat transfer through the base, as measured by the Nusselt number. It was determined that the maximum *Nu* is achieved when the relative azimuthal velocity above the base of the enclosure is zero, while the minimum *Nu* is obtained when *Fr* is approximately unity. Correspondingly, it was found that the maximum *Nu* is measured when the thermal boundary-layer thickness is at its thinnest while the velocity-boundary layer is at its thickest.

For future work, it would be interesting to explore smaller and larger values of *Q* to further investigate its relationship with *Fr*. Additionally, the linear stability of these flows should be studied to determine the effect of centrifugal buoyancy in rotating horizontal convection.

NOMENCLATURE

α	volumetric expansion coefficient
δ	change in
δ_θ	thermal boundary layer thickness
δ_u	velocity boundary layer thickness based on radial velocity
ε	relative percentage error
θ	temperature
θ_0	reference temperature
κ	thermal diffusivity
ν	kinematic viscosity
ρ	density
φ	azimuthal coordinate
Ω	rotation rate of the tank
A	tank height to radius aspect ratio
E	Ekman number
Fr	Froude number
$Fr_{Nu,\max}$	Froude number corresponding to maximum Nu
$Fr_{Nu,\min}$	Froude number corresponding to minimum Nu
$\mathbf{g}$	gravitational acceleration
$\hat{\boldsymbol{g}}$	unit vector in the direction of gravity
H	height of the tank
N_p	polynomial degree
Nu	Nusselt number
$\mathcal{O}$	order
p	pressure
Pr	Prandtl number
Q	rotational parameter
r	radial coordinate
R	radius of the tank
Ra	Rayleigh number
t	time
$\mathbf{u}$	velocity vector
$u_{\varphi,\mathrm{rel}}$	azimuthal velocity relative to the tank rotation
z	axial coordinate

ACKNOWLEDGMENTS

This research was supported by ARC Discovery grants DP150102920 and DP180102647, and was undertaken with the assistance of resources from the National Computational Infrastructure (NCI), which is supported by the Australian Government.

REFERENCES

[1] Hughes, G. O. & Griffiths, R. W. 2008 Horizontal convection. *Annu. Rev. Fluid Mech.* 40, 185–208.

[2] Mullarney, J. C., Griffiths, R. W. & Hughes, G. O. 2004 Convection driven by differential heating at a horizontal boundary. *J. Fluid Mech.* 516, 181–209.

[3] Sheard, G. J. & King, M. P. 2011 Horizontal convection: Effect of aspect ratio on Rayleigh number scaling and stability. *Appl. Math. Model.* 35 (4), 1647–1655.

[4] Tsai, T., Hussam, W. K., Fouras, A. & Sheard, G. J. 2016 The origin of instability in enclosed horizontally driven convection. *Int. J. Heat Mass Trans.* 94, 509–515.

[5] Rossby, H. T. 1965 On thermal convection driven by non-uniform heating from below: an experimental study. In *Deep-Sea Res.* vol. 12, pp. 9–16. Elsevier.

[6] Shishkina, O., Grossmann, S. & Lohse, D. 2016 Heat and momentum transport scalings in horizontal convection. *Geophys. Res. Lett.* 43 (3), 1219–1225.

[7] Hignett, P., Ibbetson, A. & Killworth, P. D. 1981 On rotating thermal convection driven by non-uniform heating from below. *J. Fluid Mech.* 109, 161–187.

[8] Barkan, R., Winters, K. B. & Smith, S. G. L. 2013 Rotating horizontal convection. *J. Fluid Mech.* 723, 556–586.

[9] Hussam, W. K., Tsai, T. & Sheard, G. J. 2014 The effect of rotation on radial horizontal convection and Nusselt number scaling in a cylindrical container. *Int. J. Heat Mass Trans.* 77, 46–59.

[10] Sheard, G. J., Hussam, W. K. & Tsai, T. 2016 Linear stability and energetics of rotating radial horizontal convection. *J. Fluid Mech.* 795, 1–35.

[11] Hart, J. E. 2000 On the influence of centrifugal buoyancy on rotating convection. *J. Fluid Mech.* 403, 133–151.

[12] Lopez, J. M., Marques, F. & Avila, M. 2013 The Boussinesq approximation in rapidly rotating flows. *J. Fluid Mech.* 737, 56–77.

[13] Karniadakis, G. E., Israeli, M. & Orszag, S. A. 1991 High-order splitting methods for the incompressible Navier–Stokes equations. *J.Comput. Phys.* 97, 414–443.

[14] Karniadakis, G. E. & Sherwin, S. J. 2005 Spectral/hp element methods for computational fluid dynamics. Numer. Math. Sci. Comp.

[15] Leigh, M. A., Tsai, T. & Sheard, G. J. 2016 Probing horizontal convection instability via perturbation of the forcing boundary layer using a synthetic jet. *Int. J. Thermal Sci.* 110, 251–260.

[16] Stern, M. E. 1975 *Ocean circulation physics*, vol. 19. Academic Press.

[17] Park, Y.-G. & Whitehead, J. A. 1999 Rotating convection driven by differential bottom heating. *J. Phys. Oceanogr.* 29 (6), 1208–1220.